

Reconciling Geophysical and Geochemical Observations of Supercontinent Insulation

Mark J. Hoggard^{a,b,*}, Oliver Shorttle^{c,d}, Fred Richards^a, Nicky White^e, John Maclennan^c

^a*Department of Earth & Planetary Sciences, Harvard University, 20 Oxford Street, Cambridge, MA 02138, USA*

^b*Lamont-Doherty Earth Observatory, Columbia University, New York, USA*

^c*Department of Earth Sciences, University of Cambridge, Downing Street, Cambridge, CB2 3EQ, UK*

^d*Institute of Astronomy, University of Cambridge, Madingley Rise, Cambridge, CB3 0HA, UK*

^e*Bullard Laboratories, University of Cambridge, Madingley Road, Cambridge, CB3 0EZ, UK*

Abstract

The thermal blanketing effect of continental lithosphere has been predicted to produce cyclical variations of upper mantle temperature during the aggregation and dispersal of supercontinents. Theoretical simulations have linked these elevated temperatures to the onset of rifting, increased magmatism and flood basalt generation, continental uplift, erosion and weathering and long term geochemical cycling. Recently, direct evidence supporting this behaviour has come from variations in the major element chemistry of mid-ocean ridge basalts (MORB), with postulated excess break-up temperatures of $\sim 150^{\circ}\text{C}$ that decay over ~ 100 Myr. Here, we have collated a database of ~ 2000 marine seismic experiments to produce a global inventory of 2340 measurements of oceanic crustal thickness, taking care to avoid areas of secondary magmatic thickening near seamounts or thinning across transform faults. These thicknesses are a proxy for mantle potential temperature at the time of melting beneath the mid-ocean ridge system, allowing quantification of the amplitude and duration of thermal anomalies generated beneath supercontinents. Jurassic breakup of Pangea formed the Atlantic and Indian Oceans, where crustal thickness trends provide statistically significant evidence for $\sim 50^{\circ}\text{C}$ regional excess temperatures that cool at a rate of $0.3\text{--}0.8^{\circ}\text{C Myr}^{-1}$. In contrast, crustal thickness measurements from the Pacific Ocean, which has not formed from rifting of a supercontinent, are approximately constant, indicating a background cooling rate of only $0.07 \pm 0.01^{\circ}\text{C Myr}^{-1}$, similar to previous estimates of secular mantle cooling. Superimposed on these longer term trends are local 50°C variations that are probably caused by background small-scale convection in the upper mantle. Two plume-influenced break-up events in the South Atlantic and Iceland provide evidence for localised excess temperatures of $\sim 150^{\circ}\text{C}$ decaying at rates of $7 \pm 1^{\circ}\text{C Myr}^{-1}$. Finally, we reconcile these updated magnitudes of supercontinental insulation with geochemically derived estimates by reinterrogating the relationship between crustal thickness and MORB compositions (Na_8) at active spreading ridges. The slope is a factor of three steeper than previously inferred, resulting in excellent agreement between both sets of observations for $\sim 50^{\circ}\text{C}$ thermal anomalies. Our global inventory of mantle temperatures through time will provide an important constraint for future numerical models of mantle convection.

Keywords: Supercontinental cycles, Continental insulation, Oceanic crustal thickness, Potential temperature, Na_8 , Mantle thermal history

1. Introduction

Episodic cycles of supercontinent assembly and break-up are thought to play a significant role in modulating heat loss from the Earth's mantle (Grigné and Labrosse, 2001; Lenardic et al., 2005). Large amalgamations of relatively slow-moving continents are expected to insulate the underlying mantle, leading to a build up of heat (Elder, 1967).

*Corresponding author

Email address: mark_hoggard@fas.harvard.edu (Mark J. Hoggard)

5 The resulting effects of these thermal anomalies have been the subject of much debate. For example, it has been noted
that Early Mesozoic assembly of Pangea occurred in the present-day location of the north African geoid high which has
been linked to hotspot locations and polar wander (Anderson, 1982). This region is associated with voluminous basalts
of the Central Atlantic Magmatic Province, which potentially contributed to environmental stress and extinction at
the Triassic-Jurassic boundary (Marzoli et al., 1999). Growth of thermal anomalies in the upper mantle beneath
10 supercontinents is likely to cause isostatic uplift and relative sea level fall (Korenaga, 2007). Furthermore, assembly
and dispersal of supercontinents may cause transitions between island-arc and continental-arc dominated subduction,
with implications for carbonate preservation, volatile release, and long-term climate cycles (Lee et al., 2013; McKenzie
et al., 2016).

The effect of continents on underlying mantle thermal structure is anticipated from their physical properties:
15 continental lithosphere has higher thermal resistance than oceanic regions due to its greater thickness and larger
radioactive heat production (Sclater et al., 1980). However, beyond this basic insight, much of our understanding of
the thermal consequences of supercontinents has been from numerical experiments. For example, build up of sub-
plate heat in simulations has been shown to cause thermal erosion of the lithosphere, which combined with surface
uplift and magmatism can lead to rifting and continental break-up (Gurnis, 1988; Guillou and Jaupart, 1995; Coltice
20 et al., 2007). Numerical models have also suggested that enhanced convective flow associated with these thermal
anomalies can propel continental rafts away from break-up locations (Elder, 1967; Zhong and Gurnis, 1993; Lowman
and Jarvis, 1993; Rolf et al., 2012). Modelling has suggested a great diversity of possible effects that continental
insulation may have on mantle dynamics and Earth's surface environment. In this contribution we provide additional
25 insight into this phenomenon by placing tighter observational constraints on the magnitude and duration of post-
breakup mantle thermal anomalies. Sub-plate temperature anomalies have a primary impact on the geochemistry
and melt productivity of mid-oceanic spreading centres. We therefore interrogate a new global compilation of oceanic
crustal thickness measurements for signals associated with continental insulation. These results are combined with
geochemical compositions of mid-ocean ridge basalts obtained from dredging on active ridges and from boreholes
drilled into Mesozoic basement to constrain the amplitude and duration of thermal anomalies caused by supercontinent
30 insulation.

2. Observations of Mantle Temperature

Despite an abundance of theoretical studies, direct observations of the large-scale temperature evolution of the
upper mantle have proven difficult to isolate. Very long-term cooling trends have been derived from the geochemistry
of non-arc basalts, komatiites and the stability of Archean continental lithosphere (Bickle, 1986; Herzberg et al., 2010).
35 These results suggest Early Proterozoic ambient mantle temperatures were elevated 150–250 °C above present-day
values, yielding ~ 0.1 °C Myr⁻¹ average cooling rates. Episodic thermal anomalies related to supercontinent cycles
are expected to act on top of this long-term secular cooling.

Higher resolution Mesozoic and Cenozoic observations have been primarily based upon measurements of mid-ocean
ridge basalt (MORB) geochemistry. Humler et al. (1999) analysed a suite of ODP and DSDP drill sites with samples of
40 oceanic basement. Careful selection criteria included removing off-axis or altered basalts, avoiding anomalously shallow
bathymetric features, selecting samples only > 80 Ma and removing exotic geochemical signatures such as hotspots.
Major and trace-element measurements on the remaining 20 sites were subsequently corrected for fractionation and
compared to modern zero-age MORB glasses. Values of Na₈ (Na₂O content corrected to 8 wt % MgO) or the trace
element proxy Sm/Yb_N (normalised to chondrites) suggest that ridge-axis temperatures have reduced by ~ 50 °C over

the last 80 Ma. Similar analysis of additional sites younger than 80 Ma indicated that the thermal anomaly decayed quickly, and mean Cenozoic mantle potential temperatures were relatively invariant (Machetel and Humler, 2003). Na_8 at the > 80 Ma drill sites and along active spreading ridges was shown to increase systematically with distance to the nearest continental margin in the Atlantic and Indian Oceans, suggesting cooling rates of 0.05–0.10 °C km⁻¹ (Humler and Besse, 2002). In contrast, the Pacific basin formed by intra-oceanic rifting in the absence of any continental insulation effects, and data in the basin showed no clear cooling trend.

Due to issues with sample alteration by seawater and the use of whole-rock geochemical analyses in these older studies, Brandl et al. (2013) repeated these measurements on a new dataset. 22 Pacific and 8 Atlantic drill sites were selected, with basement ages ranging from 6 to 170 Ma. Only fresh volcanic glasses were analysed in order to avoid the effects of alteration having potentially modified basalt Na content and crystal accumulation. Na_8 measurements show no systematic variation for Pacific samples, but Atlantic values steadily increase from 1.7 wt% at ~ 165 Ma to 2.5 wt% for samples < 100 Ma. This trend was interpreted as a 150 °C cooling event following break-up of Pangea.

Temperature variations in the MORB melting region influence total melt productivity in addition to its geochemistry (Klein and Langmuir, 1987; McKenzie and Bickle, 1988). Large upper mantle temperature anomalies that decay following continental break-up should therefore also be visible in the architecture of oceanic crust. Thicker crust should be observed for the oldest oceanic floor abutting continental margins, which then reduces in younger oceanic lithosphere towards the present-day spreading ridge. Observational studies of these crustal thickness variations have been somewhat limited. Early compilations of Pacific slope-intercept refraction experiments suggested that there may be a systematic increase in the thickness of oceanic Layer 3 at greater ages (Le Pichon, 1969; Goslin et al., 1972; Christensen and Salisbury, 1975). However, as data from anomalous regions was subsequently excluded, the amplitude of this apparent thickening through time was reduced. McClain and Atallah (1986) re-analysed old refraction results along a South Pacific transect using synthetic seismograms generated with the WKBJ algorithm (Chapman, 1978). Their results showed that previously interpreted variation was not recovered in data analysed with a more advanced modelling technique. The authors subsequently collated 100 velocity-depth profiles in the Pacific Ocean spanning from mid-Cretaceous lithosphere through to the present-day East Pacific Rise. Data over seamounts and fracture zones were avoided, and the resulting measurements indicate a minor systematic thickness reduction of only 0.34 km over this ~ 100 Ma period. If this change in thickness is assumed to result from reducing mantle potential temperatures and melt production, it is equivalent to ~ 6 °C of cooling (well within error of any petrological thermometer of mantle potential temperature). Rates of 0.06 °C Myr⁻¹ are therefore in broad agreement with long-term secular cooling trends and consistent with an absence of supercontinent insulation effects beneath the Pacific Ocean.

There are no further studies of basin-scale variations in oceanic crustal thickness until Hoggard et al. (2014), who compiled a global inventory of over 1500 modern marine seismic experiments. Their measurements indicated the presence of ~ 50 °C post-break-up cooling events in the Atlantic and Indian Oceans, and confirmed the lack of a systematic variation in Pacific data. Excess temperatures were observed to decay exponentially with characteristic folding times of ~ 50 Ma in the Central and South Atlantic data (Hoggard et al., 2016a). These observations were subsequently tested by Van Avendonk et al. (2017) using their own compilation of 234 wide-angle refraction experiments. This latter study confirmed the presence of ~ 50 °C excess temperatures in the oldest ocean floor in the central Atlantic Ocean, and estimated mean cooling rates of 0.15–0.20 °C Myr⁻¹ since the Jurassic period.

Here, we have chosen to re-examine existing observations of oceanic crustal thickness in order to quantify the amplitude and duration of thermal anomalies that build up beneath supercontinents. We then seek to reconcile the current post-break-up excess temperatures of ~ 50 °C based upon crustal thickness measurements with > 150 °C values derived from the latest geochemical observations.

3. Crustal Thickness Database

Over the last 20 years, there has been a steady improvement in acquisition and processing techniques of marine seismic reflection profiles, primarily driven by the hydrocarbon industry. The density and quality of regional-scale experiments has increased dramatically, particularly along passive continental margins. These data image crustal architecture in striking detail. Structures interpreted include seaward dipping reflectors, seamounts, lower crustal reflectivity, faulting and fracture zones (e.g. Figure 1). Reflections from the sediment-basement interface and Moho allow high resolution variations in the thickness of oceanic crust to be locally mapped.

In this study, we primarily exploit oceanic crustal thickness measurements from a recent global compilation of ~ 2000 marine seismic experiments (Hoggard et al., 2017). Approximately two-thirds of these measurements are derived from multi-channel reflection profiles, complemented with ~ 700 wide-angle refraction experiments of varying vintages. Where necessary, crustal thickness was converted from two-way travel time into true thickness using a constant velocity of $6.32 \pm 0.35 \text{ km s}^{-1}$. This value was calculated from 149 velocity-depth profiles through oceanic crust derived from modern wave-modelled wide-angle experiments. Many pre-1990 refraction experiments were analysed using the slope-intercept modelling technique, which typically under-predicts crustal thickness by $\sim 20\%$ (White et al., 1992). However, these points are often the only data available towards the centre of large ocean basins. Fully-reversed experiments have therefore been included within our database for completeness, but are not used in any of the analysis.

Measurements of primary crustal thickness are required in order to interpret data in terms of mantle melting conditions beneath the spreading ridge axis at time of formation. However, significant volumes of basaltic material are also added off-axis to the crust by hotspot volcanism in the form of seamounts. A prime example is the Hawaiian-Emperor chain in the Pacific Ocean. Such regions are not desired in our analysis and must be filtered from the database. One method is to use plate-reconstruction models to predict the paths of present-day hotspots through time and remove any nearby measurements (e.g. Van Avendonk et al., 2017). However, this approach introduces significant uncertainty into the results relating to choice of reconstruction model and relative hotspot motions. Our preferred technique is to carefully identify and map areas of anomalous ocean floor affected by seamount volcanism using high resolution maps of bathymetry and free-air gravity anomalies derived from satellite altimetry. An additional advantage of this method is that major fracture zones, where crust has undergone post-emplacement brittle thinning, are also removed. Detailed maps showing these polygons are included in the Supporting Information. In addition, large seamounts and fracture zones have been avoided where possible during interpretation of the original seismic experiments. Finally, all thickness measurements are averaged within 0.5° bins, in order to smooth out any minor local features.

The database of crustal thickness measurements contains 2340 accurate measurements and 359 minimum constraints from vintage slope-intercept refraction experiments (Figure 2). The majority of measurements range between 12 km and 4 km, with a mean and standard deviation for the most accurate observations (circles only) of $6.9 \pm 2.2 \text{ km}$ versus $6.0 \pm 1.7 \text{ km}$ for the minima derived from slope-intercept data. There is good data coverage along the passive margins of the Atlantic and Indian Oceans. Data in the Pacific Ocean is concentrated on old ocean floor in the northwest and along the Aleutian, Cascadian, Middle American and Peru-Chile subduction zones. Locations with the most limited coverage are central regions of the South Pacific and South Atlantic Oceans.

4. Thickness versus Spreading Rate

A key observation that provides support for the corner flow model of mid-oceanic spreading centres comes from the relationship between crustal thickness and spreading rate (Reid and Jackson, 1981). Crustal thickness is expected

to be relatively constant at half-spreading rates $> 15 \text{ mm yr}^{-1}$ and steadily reduce to zero for slower spreading rates as the vertical flow of hot mantle is sufficiently gradual for it to cool by conduction during upwelling (Bottinga and Allegre, 1978; Bown and White, 1994).

In Figure 3a we test the spreading rate-crustal thickness relationship. Half-spreading rates are assigned to the crustal thickness measurements using the magnetic reversal history of Müller et al. (2008), and have been binned into 5 mm yr^{-1} blocks. The mean value for each bin is consistently $< 1 \text{ km}$ from the global mean thickness of 6.88 km but has wide standard deviations of 0.8–2.7 km. There is no obvious correlation between spreading rate and crustal thickness. Even at slow spreading rates, any drop-off to thinner values is masked by the large amount of scatter in the data. This scatter is likely to reflect changes in potential temperature beneath ridge axes related to small-scale convection in the upper mantle, which is probably the dominant effect.

An important caveat to the above analysis is that the spreading rate grid is generated by differentiating the oceanic age grid along flow lines (Müller et al., 2008). It is therefore susceptible to noise generated either by incorrect picks of magnetic anomalies or from the necessary assignment of constant spreading rates between picks (for example in the mid-Cretaceous superchron). These effects are likely to introduce significant scatter into the half-spreading rates and may mask the slow spreading rate-crustal thickness signal if its onset is at half-spreading rates $\leq 10 \text{ mm yr}^{-1}$.

In order to avoid issues with spreading rate grids, a subset of 66 crustal thickness measurements on active spreading ridges have been selected. These points all lie on crust younger than 10 Ma and are also less than 200 km from the ridge. Data have been averaged over each spreading segment to reduce the effects of variable melt supply along the segment (e.g. White et al., 2001). Segments and spreading rates are taken from the global compilation of Gale et al. (2013), which used the NUVEL-1A and NR-MORVEL56 plate rotation models (DeMets et al., 1994; Argus et al., 2011). The familiar behaviour becomes much more apparent (Figure 3b). There is a steady increase in crustal thickness up to $\sim 10 \text{ mm yr}^{-1}$ half-spreading rates. This trend is dominated by the Mohns and Gakkel ridges, along with two points from the Southwest Indian Ridge. The cluster of high crustal thicknesses are predominantly less than 1000 km from Iceland and are influenced by excess temperatures of the Icelandic plume. Above 10 mm yr^{-1} half-spreading rates, the data show no systematic change in crustal thickness, although the scatter steadily reduces. This behaviour has been observed previously and linked to the higher density of transform faults on slow spreading ridges, resulting in a more three-dimensional crustal accretion (Chen, 1992). However, there is also a sampling bias because there is a longer length of active ridges available at slower spreading rates (see histogram along base of Figure 3b). The larger range of crustal thicknesses may therefore partly arise due to the increased likelihood of sampling a range of localised asthenospheric temperature variations related to small-scale convection in the upper mantle at slower spreading rates.

We have performed a statistical test to further investigate the relative importance of this sampling bias. The standard deviation of crustal thickness measurements for ridges with half-spreading rates between 15–45 mm yr^{-1} is approximately a factor of 2.5 larger than that for 45–75 mm yr^{-1} spreading centres. In order to test whether this is a result of the wider spatial distribution of intermediate spreading ridges sampling a larger range of potential temperatures, a proxy for asthenospheric temperature variations is required. Here, we adopt the global dynamic topography grid of Hoggard et al. (2016b) as the 1000 km surface deflections typically observed are predominantly caused by buoyancy in the uppermost mantle and have been shown to correlate well with seismic tomographic images beneath the plate. This grid has been randomly rotated 1 million times and sampled using the present-day distribution of mid-oceanic ridges at 1 km intervals. The standard deviation of dynamic topography for ridges with half-spreading rates between 15–45 mm yr^{-1} is computed and compared with that of 45–75 mm yr^{-1} spreading centres. In only 0.001% of cases does the reduction between the two bins match or exceed the observed drop of a factor of 2.5. Thus we infer that sampling bias is not the primary cause of the reduced spread in crustal thicknesses observed in Figure 3b, in

support of the concept of a transition from three-dimensional to two-dimensional crustal accretion style with increasing
170 spreading rate (Chen, 1992).

5. Potential Temperature through Time

Crustal thickness can be related to mantle potential temperature using a parameterisation for melting (Supplementary Information). Here, we have adopted the model of Shorttle et al. (2014) which assumes isentropic decompression and fractional melting over a triangular melt region. The solidus and liquidus are taken as the anhydrous KLB-1
175 lherzolite source (Katz et al., 2003). Melts are instantaneously and completely extracted, and the top of the melting column is calculated to be the point at which the pressure of overlying crust is equal to the upwelling pressure. This parameterisation produces 6.9 km of oceanic crust for a mantle potential temperature of $T_p = 1330$ °C. The 4–12 km typical range of crustal thicknesses are produced by $T_p = 1278$ –1399 °C. Inferred changes in mantle potential temperature are robust with respect to alternative MORB melting models. However, absolute temperatures are dependent
180 on the choice of heat capacity, entropy of fusion, and peridotite solidus used in the melting model. Thus, we have chosen to emphasise relative changes in temperature occurring along the flow lines, which are less sensitive to these choices.

Crustal thickness data have been separated into individual basins to investigate the temporal evolution of regional upper mantle temperature variations. The break-up of Pangea initiated in the late Triassic period when rifting in the
185 interior of the supercontinent between Gondwana and North America began to form the present-day central Atlantic Ocean (Müller et al., 2016). The margins of eastern North America and northwestern Africa probably have the best temporal resolution of crustal thickness variations within the database, with good coverage from ~190 Ma ocean floor through to 120 Ma on both conjugate flanks. All accurate observations located north of Vema fracture zone and south of the Pico fracture zone are plotted in Figure 4a. Crustal thicknesses steadily reduce from ~9 km to ~7 km throughout this period on both margins, giving approximate cooling rates of 30 °C per 100 Myr. There is significant scatter in the data that has a similar amplitude to the background cooling signal. This scatter may be generated by a range of factors including spreading rate changes, along-segment variations in melt supply and local upper mantle temperature anomalies. Notably, removing data with a half-spreading rate < 10 mm yr⁻¹ in the Müller et al. (2008)
190 grid does not reduce the scatter for this or any of the other regions considered. Furthermore, averaging the thickness measurements over wider bins also has limited effect, suggesting segment-scale structure is not the source. The most likely cause is local variations in sub-plate temperature related to small-scale convection in the upper mantle, which appear to have amplitudes of ±50 °C.

Given this scatter in observed potential temperature at any given time arising from other geological processes, it is important to estimate the significance of fitting a cooling trend to the data. We have therefore performed F-tests on
200 each of the datasets. The test involves stating a null hypothesis that a model with zero slope provides an adequate fit to the potential temperature estimates. This model is fitted to the data and the sum of squared residuals is computed and compared to that of the model with a linear slope. F-test values > 1 indicate that the variance is significantly reduced by adding a slope. The associated p-value estimates the probability that this F-statistic might be recovered by chance if the null hypothesis were true. Therefore high F-tests with low p-values indicate that the null hypothesis should be rejected in place of the linear model. Applying these statistical tests to the 163 measurements used to constrain cooling following rifting of North America and Gondwana gives an F-test value of 54 and associated p-value of < 0.01%. This result suggests that there is a significant cooling trend contained within the observations.

Around the same time in the early Jurassic period, a rift opened up on the eastern margin of Pangea between west

Table 1: Recovered cooling trends and statistical tests.

Rifting Episode	Figure	Slope ($^{\circ}\text{C Myr}^{-1}$)	No. of data	F-test	p-value
N. America–Gondwana	4a	0.26 ± 0.04	163	54.0	9.47×10^{-12}
East–West Gondwana	4b	0.75 ± 0.15	91	24.1	4.15×10^{-6}
East Gondwana	4c	0.29 ± 0.03	356	84.4	3.57×10^{-18}
West Gondwana	4d	0.82 ± 0.09	383	88.6	4.73×10^{-19}
Pacific Ocean	5	0.07 ± 0.01	294	24.9	1.03×10^{-6}
Walvis–Rio Grande	6a	7.64 ± 0.78	29	95.3	2.38×10^{-10}
Reykjanes	6b	6.93 ± 1.75	38	15.8	3.28×10^{-4}

and east Gondwana (separating present-day east Africa from the landmass containing Madagascar, India, Antarctica and Australia). There are substantially fewer observations of crustal thickness along East Africa, with most of the data concentrated off the northwest coast of Madagascar and along the margins of Kenya and Tanzania. The area of oceanic floor considered for this event is bounded in the north by the Chain Ridge between the Somali Basin and Arabian Sea which runs down to Madagascar (Figure 2). The southern extent is bounded by the Shaka and Indomed Fracture Zones in the west and east respectively. Unfortunately, much of the southern data is restricted to the Agulhas Plateau and Maud Rise – LIPs thought to be generated by the Bouvet hotspot. This data has therefore been removed as it is probably not representative of general background oceanic crust. The subsequent compilation of thicknesses on crust older than 150 Ma appears to be on average ~ 25 $^{\circ}\text{C}$ warmer than data from 140–120 Ma. However, limited coverage renders this trend somewhat unconvincing. Interestingly, the absolute temperature at rifting is 20–30 $^{\circ}\text{C}$ cooler than in the central Atlantic Ocean. This may reflect less effective insulation of the upper mantle towards the periphery of the Pangean supercontinent, where heat could escape through the adjacent oceanic lithosphere of the Neotethys Ocean.

Break-up of east Gondwana began with the present-day northwest shelf of Australia, shortly followed by early Cretaceous rifting between east India and Antarctica. This break-up culminated with late Cretaceous separation of Australia from Antarctica and India from Madagascar, the latter of which was punctuated by the Deccan Traps LIP. Oceanic lithosphere created during these events makes up the majority of the modern Indian Ocean, although significant quantities of the Somali and northwest Australian conjugate flanks have now been subducted at the Makran and Java subduction zones. Thickness measurements have been selected that lie east of Chain Ridge, the Owen and Indomed Fracture Zones all the way across the Australian-Antarctic Discordance upto the Balleny Fracture Zone. Again, the data exhibit a large amount of scatter, but there is a gradual decrease in mean potential temperature of approximately 50 $^{\circ}\text{C}$ from oldest to youngest, yielding cooling rates of ~ 30 $^{\circ}\text{C}$ per 100 Myr. These 356 data points have an F-test value of 84 and associated p-value of $< 0.01\%$, suggesting that this cooling trend is significant. Notably, the oldest crust around the northwest shelf of Australia suggests potential temperatures of 1340 $^{\circ}\text{C}$ at 150 Ma, in close agreement with Central Atlantic values and ~ 25 $^{\circ}\text{C}$ warmer than the east African data.

The final major oceanic basin formed as a result of Pangean rifting is the South Atlantic Ocean. Early Cretaceous break-up of West Gondwana began in the south and steadily progressed northwards as South America separated from Africa. The Paraná-Etendeka flood basalts are a LIP sourced from the proto-Tristan da Cunha plume and are contemporaneous with initial stages of this opening. The plume remained approximately on the spreading axis, creating the ~ 500 km wide aseismic ridges known as the Walvis and Rio-Grande Rise. Temporal coverage is enhanced by the

diachronous opening of the basin, with seismic profiles offshore Argentina and Namibia constraining early behaviour
240 whilst profiles around Equatorial Brazil and west Africa cover the later stages. However, this architecture also results in a systematic northwards shift of the sampling location through time. Selected measurements lie between the Doldrums and Falklands-Agulhus Fracture Zones to the north and south, respectively. Data from the immediate vicinity of the Walvis and Rio-Grande Rise have been excluded. The results are shown in Figure 4d and despite wide scatter, suggest gradual cooling from approximately 1340 °C at 125 Ma down to ~ 1300 °C by 70 Ma. Measurements are roughly
245 consistent from each of the conjugate flanks (black versus grey points). These 383 datapoints yield an F-test value of 89 and p-value < 0.01% indicating a significant cooling trend. However, the slope of $\sim 0.8 \pm 0.1$ °C Myr⁻¹ is 2–3 times larger than results for North American–Gondwanan break-up and rifting of East Gondwana. Given that initial excess temperatures are similar for all three regions, this result might indicate that the thermal anomaly was less widespread and so cooled faster beneath the South Atlantic Ocean.

If excess temperature anomalies are generated by the insulatory affects of Pangea, an important corollary is that
250 measurements in the Pacific Ocean should not exhibit large cooling trends. Pacific observations tend to come from wide-angle refraction experiments, with modern profiles often clustered at subduction zones and active spreading ridges, backed up by sparse vintage slope-intercept experiments in the central basin. Additionally, there is good coverage on Mesozoic seafloor in the west towards Japan. These data are collated in Figure 5. Similar amplitudes of
255 scatter are observed as in the previous basins, but the mean value is ~ 1325 °C and is relatively invariant through time. This result is consistent with a lack of excess temperature anomaly beneath the Pacific Ocean, where the majority of ocean floor formed > 2000 km from the nearest continental margin. The recovered cooling rates are $\sim 7 \pm 1$ °C per 100 Myr, which is remarkably similar to long-term secular cooling trends derived from the geochemistry of non-arc basalts, komatiites and the stability of Archean continental lithosphere (Bickle, 1986; Herzberg et al., 2010).

260 6. Cooling trends of Plumes

There are two regions within the database where there is good temporal coverage of rifting events strongly influenced by mantle plumes. First, the Tristan da Cunha plume caused widespread basaltic volcanism covering Paraná and Etendeka during rifting of the South Atlantic Ocean. $^{40}\text{Ar}/^{39}\text{Ar}$ dating gives an apparent age of 133 ± 1 Ma, shortly predating the oldest magnetic anomalies in the oceanic crust (Renne et al., 1992; Rabinowitz and LaBrecque, 1979).
265 Geochemical analyses of ultra-magnesian olivines from Etendeka volcanics indicate excess melting temperatures of ~ 1520°C (Keiding et al., 2011; Herzberg, 2011).

Two areas of anomalous oceanic crust have been mapped using high resolution gravity and bathymetry data. The Rio Grande Rise marks excess volcanism on the South American flank, whilst the Walvis Ridge sits on the African side. A small subset of oceanic crustal thickness observations fall within these regions, biased towards the South
270 American margin where there is a higher density of seismic reflection profiles. The oldest ocean floor abutting the continental margin is abnormally thick (up to 4 seconds two-way travel time) and characterised by stacked seaward dipping reflectors (SDRs) that are caused by widespread basalt flows. Compiling all data in the vicinity of the Walvis and Rio-Grande Rises suggests that the earliest oceanic crust records excess temperatures of up to 1480 °C which rapidly decays over 20 Myr, giving cooling rates of ~ 7 °C Myr⁻¹ (Figure 6a). This cooling is more than an order of
275 magnitude faster than the apparent background cooling rate in the rest of the Atlantic Ocean.

The second plume-influenced break-up with excellent data coverage is in the North Atlantic Ocean in the vicinity of Iceland. There are a high density of modern refraction experiments on the southeast margin of Greenland and western margin of the Faeroe-Hatton Bank shelf. This oceanic floor was generated at the Reykjanes Ridge, and

thick SDR sequences and the pattern of propagating V-shaped ridges indicate the influence of the proto-Icelandic plume beginning at 65 Ma and continuing until the present-day (Vogt, 1971; Parnell-Turner et al., 2017). Thickness measurements adjacent to the margins have been compiled that lie between the Bight Fracture Zone in the south and Greenland-Iceland-Faeroe Rise to the north (Figure 6b). Observations suggest initial excess temperatures of up to 200 °C occurred over a widespread area. Away from the central plume conduit, this temperature anomaly appears to decay over the following 20 Myr at rates of > 10 °C Myr⁻¹. Thermal anomalies associated with plume head material therefore are both hotter and probably thinner, resulting in more rapid cooling, than those associated with supercontinent insulation.

7. Discussion

Variations in oceanic crustal thickness indicate that there may be elevated upper mantle temperature anomalies of ~ 50 °C following break-up of Pangea. This value is three-times lower than recent estimates derived from Na₈ thermometry on MORB samples from Atlantic drill sites (Brandl et al., 2013). It is therefore necessary to reinvestigate these geochemical constraints.

The relationship between Na₈ and potential temperature can be recalibrated using crustal thickness measurements taken from active ridges with associated zero-age dredge samples. Thickness observations have been limited to those on lithosphere younger than 5 Ma and are averaged along each spreading segment. A subset of 45 of these points are subsequently selected that occur less than 300 km from a segment with geochemical measurements, using the dredge sample compilation of Gale et al. (2014). There is a good correlation between crustal thickness and Na₈ values, with a Pearson's correlation coefficient of ~ 0.8 (Figure 7b). A simple linear fit to the data gives

$$\text{Na}_8 \approx -0.23 z_c + 4.05 \quad (1)$$

where Na₈ is fractionation-corrected sodium oxide in weight % and z_c is the crustal thickness in kilometres. This updated relationship can be applied to the Na₈ values obtained in the Brandl et al. (2013) study to estimate the expected igneous crustal thickness at each of these 8 Atlantic drill sites. Conversion into potential temperature using the same relationship applied to the direct observations of crustal thickness suggests that the excess temperature following break-up of Pangea is only ~ 50 °C (Figure 7c). Importantly, the slope ($\frac{d\text{Na}_8}{dz_c}$) is approximately four times greater than that obtained by fitting a linear relationship to the data of Brandl et al. (2013). Thus, using our new calibration the observed range of Na₈ values is converted into a significantly smaller excess temperature. The ~ 50 °C thermal anomaly inferred from seismic observations is therefore in complete agreement with that derived from geochemical measurements of Na₈.

The geochemical observations used by Brandl et al. (2013) and reinvestigated here come from 8 Atlantic drill sites, seven of which are in the central Atlantic Ocean between North America and northwest Africa and the eighth is on 35 Ma oceanic crust west of the Walvis Ridge (Supplementary Information). Given the large scatter in observed seismic crustal thickness measurements caused by variations in spreading rate, sub-plate temperatures, source heterogeneity and variable melt supply along a segment, it is perhaps surprising that there is any systematic signal recovered in the Na₈ data. This result suggests that Na₈ may be less affected by these other processes and potentially a more reliable record of melting conditions than total crustal thickness.

Correlation of crustal thickness with other zero-age, fractionation-corrected oxides is less clear. Fe₈, Ca₈, Al₈ and P₈ all have Pearson's correlation coefficients of ~ 0.6, whilst only poor correlation is observed for Si₈, Ti₈ and K₈ (Supplementary Information). The relatively strong relationship between Na₈ and crustal thickness is surprising in

comparison to these other incompatible elements (e.g. K, Ti), which should behave more simply during differentiation and melting. One factor behind this behaviour is analytical precision, with the smaller concentration elements such as potassium yielding larger measurement uncertainties. However, we also tentatively suggest that the increasing stability of the jadeite component of clinopyroxene with pressure may lead to increased compatibility of Na with depth (Blundy et al., 1995). Thus deeper melt zones at higher potential temperatures produce melts with reduced sodium concentrations, which is compounded by the overall larger melt fraction which further dilutes the Na content.

8. Conclusions

A comprehensive global database of ~ 1500 high-accuracy oceanic crustal thickness measurements has been compiled and used to infer potential temperatures beneath the ridge axis at time of formation. Regional analysis reveals statistically significant divergences in mantle cooling history between the Pacific Ocean and other ocean basins that are consistent with the hypothesised phenomenon of supercontinent insulation. Pacific spreading has occurred far from sites of former supercontinent assembly, and crustal thickness trends yield a background secular cooling rate of $\sim 0.07 \pm 0.01 \text{ }^{\circ}\text{C Myr}^{-1}$, in excellent agreement with previous estimates. In contrast, the Atlantic and Indian basins formed by the breakup and dispersal of the Pangaea supercontinent throughout the Jurassic and Cretaceous periods and exhibit crustal thickness variations that record a systematic $\sim 50\text{ }^{\circ}\text{C}$ temperature excess that cools significantly faster ($\sim 0.3\text{--}0.8 \text{ }^{\circ}\text{C Myr}^{-1}$). In addition, two regions that record plume-influenced break-up in the South Atlantic Ocean and around Iceland exhibit initial excess temperatures of $\sim 150 \text{ }^{\circ}\text{C}$ and cooling rates that are an order of magnitude faster again ($7 \pm 1 \text{ }^{\circ}\text{C Myr}^{-1}$).

Thermal anomalies of $\sim 50\text{ }^{\circ}\text{C}$ associated with supercontinent assembly are a factor of three smaller than recent estimates derived from sodium oxide concentrations in mid-ocean ridge basalts from 8 Atlantic drill sites. However recalibrating the Na_8 versus crustal thickness relationship using 45 thickness measurements at modern spreading centres yields revised Na_8 excess temperature estimates that are in agreement with this lower value.

Analysis of the relationship between crustal thickness and axial ridge depth yields a steeper gradient than expected from pure crustal isostasy. Thus, inferences of crustal thickness derived from water depth at spreading centres must take into account the additional effect of dynamic topography, which is positively correlated with excess mantle temperatures and larger melt fractions.

Finally, convective simulations have proven to be an important tool for investigating temporal evolution of the Earth's mantle. Our crustal thickness database places some constraints on the expected amplitude and duration of four different thermal behaviours: long-term secular cooling, supercontinent insulation cycles, plume-influenced rifting events and background small scale convection in the upper mantle. We hope that our new database of point measurements of potential temperature through time can provide a useful boundary condition for reconstructing past mantle states throughout the Mesozoic and Cenozoic Eras.

References

- 350 Anderson, D.L., 1982. Hotspots, polar wander, Mesozoic convection and the geoid. doi:10.1038/297391a0.
- Argus, D.F., Gordon, R.G., Demets, C., 2011. Geologically current motion of 56 plates relative to the no-net-rotation reference frame. *Geochemistry, Geophysics, Geosystems* 12. doi:10.1029/2011GC003751.
- Bickle, M.J., 1986. Implications of melting for stabilisation of the lithosphere and heat loss in the Archaean. *Earth and Planetary Science Letters* 80, 314–324. doi:10.1016/0012-821X(86)90113-5.
- 355 Blundy, J.D., Falloon, T.J., Wood, B.J., Dalton, J.A., 1995. Sodium partitioning between clinopyroxene and silicate melts. *Journal of Geophysical Research* 100, 15501–15515.
- Bottinga, Y., Allegre, C.J., 1978. Partial melting under spreading ridges. *Philosophical Transactions of the Royal Society of London A* 288, 501–525.
- Bown, J.W., White, R.S., 1994. Variation with spreading rate of oceanic crustal thickness and geochemistry. *Earth and Planetary Science Letters* 121, 435–449. doi:10.1016/0012-821X(94)90082-5.
- 360 Brandl, P.A., Regelous, M., Beier, C., Haase, K.M., 2013. High mantle temperatures following rifting caused by continental insulation. *Nature Geoscience* 6, 391–394. doi:10.1038/ngeo1758.
- Chapman, C.H., 1978. A new method for computing synthetic seismograms. *Geophysical Journal of the Royal Astronomical Society* 54, 481 – 518.
- 365 Chen, Y.J., 1992. Oceanic crustal thickness versus spreading rate. *Geophysical Research Letters* 19, 753–756. doi:10.1029/92gl00161.
- Christensen, N.I., Salisbury, M.H., 1975. Structure and constitution of the lower oceanic crust. *Reviews of Geophysics and Space Physics* 13, 57–86. doi:10.1029/RG013i001p00057.
- Coltice, N., Phillips, B.R., Bertrand, H., Ricard, Y., Rey, P., 2007. Global warming of the mantle at the origin of flood basalts over supercontinents. *Geology* 35, 391–394. doi:10.1130/G23240A.1.
- 370 DeMets, C., Gordon, R.G., Argus, D.F., Stein, S., 1994. Effects of recent revision to the geomagnetic reversal timescale on estimates of current plate motion. *Geophysical Research Letters* 21, 2191–2194.
- Elder, J., 1967. Convective Self-propulsion of Continents. *Nature* 214, 657–750.
- Gale, A., Dalton, C.A., Langmuir, C.H., Su, Y., Schilling, J.G., 2013. The mean composition of ocean ridge basalts. *375 Geochemistry, Geophysics, Geosystems* 14, 489–518. doi:10.1029/2012GC004334.
- Gale, A., Langmuir, C.H., Dalton, C.A., 2014. The global systematics of ocean ridge basalts and their origin. *Journal of Petrology* 55, 1051–1082. doi:10.1093/petrology/egu017.
- Goslin, J., Beuzart, P., Francheteau, J., Le Pichon, X., 1972. Thickening of the oceanic layer in the Pacific Ocean. *Marine Geophysical Researches* 1, 418–427.
- 380 Grigné, C., Labrosse, S., 2001. Effects of continents on Earth cooling: thermal blanketing and depletion in radioactive elements. *Geophysical Research Letters* 28, 2707–2710. doi:10.1029/2000GL012475.

Guillou, L., Jaupart, C., 1995. On the effect of continents on mantle convection. *Journal of Geophysical Research* 100, 24217–24238.

Gurnis, M., 1988. Large-scale mantle convection and the aggregation and dispersal of supercontinents. *Nature* 332, 695–699. doi:10.1038/332695a0.

385 Herzberg, C., Condé, K., Korenaga, J., 2010. Thermal history of the Earth and its petrological expression. *Earth and Planetary Science Letters* 292, 79–88. doi:10.1016/j.epsl.2010.01.022.

Herzberg, C.T., 2011. Basalts as temperature probes of Earth's mantle. *Geology* 39, 1179–1180.

Hoggard, M.J., Shorttle, O., White, N., 2016a. Testing Predictions of Continental Insulation using Oceanic Crustal 390 Thicknesses. *Geophysical Research Abstracts* 18, 16611.

Hoggard, M.J., White, N.J., Al-Attar, D., 2016b. Global dynamic topography observations reveal limited influence of large-scale mantle flow. *Nature Geoscience* 9, 456–463. URL: <http://www.nature.com/doifinder/10.1038/ngeo2709>, doi:10.1038/ngeo2709.

395 Hoggard, M.J., White, N.J., Shorttle, O., 2014. Global Mantle Potential Temperature History from Oceanic Crustal Thicknesses. Abstract T33B-4680 presented at 2014 Fall Meeting, AGU, San Francisco, Calif., 15–19 Dec .

Hoggard, M.J., Winterbourne, J., Czarnota, K., White, N., 2017. Oceanic residual depth measurements, the plate cooling model, and global dynamic topography. *Journal of Geophysical Research: Solid Earth* 122, 2328–2372. doi:10.1002/2016JB013457.

Humler, E., Besse, J., 2002. A correlation between mid-ocean-ridge basalt chemistry and distance to continents. 400 *Nature* 419, 607–609. doi:10.1038/nature01052.

Humler, E., Langmuir, C., Daux, V., 1999. Depth versus age: new perspectives from the chemical compositions of ancient crust. *Earth and Planetary Science Letters* 173, 7–23. doi:10.1016/S0012-821X(99)00218-6.

Katz, R.F., Spiegelman, M., Langmuir, C.H., 2003. A new parameterization of hydrous mantle melting. *Geochemistry, Geophysics, Geosystems* 4. doi:10.1029/2002GC000433.

405 Keiding, J.K., Trumbull, R.B., Veksler, I.V., Jerram, D.A., 2011. On the significance of ultra-magnesian olivines in basaltic rocks. *Geology* 39, 1095–1098. doi:10.1130/G32214.1.

Klein, E.M., Langmuir, C.H., 1987. Global Correlations of Ocean Ridge Basalt Chemistry with Axial Depth and Crustal Thickness. *Journal of Geophysical Research* 92, 8089–8115.

410 Korenaga, J., 2007. Eustasy, supercontinental insulation, and the temporal variability of terrestrial heat flux. *Earth and Planetary Science Letters* 257, 350–358. doi:10.1016/j.epsl.2007.03.007.

Le Pichon, X., 1969. Models and structure of the oceanic crust. *Tectonophysics* 7, 385–401. doi:10.1016/0040-1951(69)90008-0.

415 Lee, C.T.A., Shen, B., Slotnick, B.S., Liao, K., Dickens, G.R., Yokoyama, Y., Lenardic, A., Dasgupta, R., Jellinek, M., Lackey, J.S., Schneider, T., Tice, M.M., 2013. Continental arc-island arc fluctuations, growth of crustal carbonates, and long-term climate change. *Geosphere* 9, 21–36. doi:10.1130/GES00822.1.

Lenardic, A., Moresi, L.N., Jellinek, M.A., Manga, M., 2005. Continental insulation, mantle cooling, and the surface area of oceans and continents. *Earth and Planetary Science Letters* 234, 317–333. doi:10.1016/j.epsl.2005.01.038.

Lowman, J.P., Jarvis, G.T., 1993. Mantle convection flow reversals due to continental collisions. *Geophysical Research Letters* 20, 2087–2090. doi:10.1029/93GL02047.

Machetel, P., Humler, E., 2003. High mantle temperature during Cretaceous avalanche. *Earth and Planetary Science Letters* 208, 125–133. doi:10.1016/S0012-821X(03)00041-4.

Marzoli, A., Renne, P.R., Piccirillo, E.E.M., Ernesto, M., Bellieni, G., De Min, A., 1999. Extensive 200-Million-Year-Old Continental Flood Basalts of the Central Atlantic Magmatic Province. *Science* 284, 616–618. doi:10.1126/science.284.5414.616.

McClain, J.S., Atallah, C.A., 1986. Thickening of the oceanic crust with age. *Geology* 14, 574–576.

McKenzie, D.P., Bickle, M.J., 1988. The Volume and Composition of Melt Generated by Extension of the Lithosphere. *Journal of Petrology* 29, 625–679. doi:10.1093/petrology/29.3.625.

McKenzie, N.R., Horton, B.K., Loomis, S.E., Stockli, D.F., Planavsky, N.J., Lee, C.T.A., 2016. Continental arc 430 volcanism as the principal driver of icehouse-greenhouse variability. *Science* 352, 444–447. doi:10.1126/science.aad5787, arXiv:1604.06419.

Müller, R.D., Sdrolias, M., Gaina, C., Roest, W.R., 2008. Age, spreading rates, and spreading asymmetry of the world's ocean crust. *Geochemistry, Geophysics, Geosystems* 9. doi:10.1029/2007GC001743.

Müller, R.D., Seton, M., Zahirovic, S., Williams, S.E., Matthews, K.J., Wright, N.M., Shephard, G.E., Maloney, K.T., Barnett-moore, N., Bower, D.J., Cannon, J., 2016. Ocean basin evolution and global-scale reorganization events since Pangea breakup. *Annual Review of Earth and Planetary Science Letters*, 107–138doi:10.1146/annurev-earth-060115-012211.

NGDC, 2006. 2-minute Gridded Global Relief Data (ETOPO2) v2.

Parnell-Turner, R., White, N., Henstock, T.J., Jones, S.M., Maclennan, J., Murton, B.J., 2017. Causes and Consequences of Diachronous V-Shaped Ridges in the North Atlantic Ocean. *Journal of Geophysical Research: Solid Earth* 122, 8675–8708. doi:10.1002/2017JB014225.

Rabinowitz, P.D., LaBrecque, J., 1979. The Mesozoic South Atlantic Ocean and Evolution of Its Continental Margins. *Journal of Geophysical Research* 84, 5973–6002. doi:10.1029/JB084iB11p05973.

Reid, I., Jackson, H.R., 1981. Oceanic spreading and crustal thickness. *Marine Geophysical Researches* 5, 165–172. 445 doi:10.1007/BF0016347.

Renne, P.R., Ernesto, M., Pacca, I.G., Coe, R.S., Glen, J.M., Prévot, M., Perrin, M., 1992. The age of Paraná flood volcanism, rifting of Gondwanaland, and the Jurassic-Cretaceous boundary. *Science* 258, 975–979. doi:10.1126/science.258.5084.975.

Rolf, T., Coltice, N., Tackley, P.J., 2012. Linking continental drift, plate tectonics and the thermal state of the Earth's mantle. *Earth and Planetary Science Letters* 351-352, 134–146. doi:10.1016/j.epsl.2012.07.011.

- Sclater, J.G., Jaupart, C., Galson, D., 1980. The heat flow through oceanic and continental crust and the heat loss of the Earth. *Reviews of Geophysics and Space Physics* 18, 269–311. doi:10.1029/RG018i001p00269.
- Shorttle, O., MacLennan, J., Lambart, S., 2014. Quantifying lithological variability in the mantle. *Earth and Planetary Science Letters* 395, 24–40. doi:10.1016/j.epsl.2014.03.040.
- ⁴⁵⁵ Van Avendonk, H.J.A., Davis, J.K., Harding, J.L., Lawver, L.A., 2017. Decrease in oceanic crustal thickness since the breakup of Pangaea. *Nature Geoscience* 10, 58–61. doi:10.1038/ngeo2849.
- Vogt, P.R., 1971. Asthenosphere motion recorded by the ocean floor south of Iceland. *Earth and Planetary Science Letters* 13, 153–160. doi:10.1016/0012-821X(71)90118-X.
- White, R.S., McKenzie, D.P., O’Nions, R.K., 1992. Oceanic Crustal Thickness From Seismic Measurements and Rare ⁴⁶⁰ Earth Element Inversions. *Journal of Geophysical Research* 97, 19,683–19,715.
- White, R.S., Minshull, T.A., Bickle, M.J., Robinson, C.J., 2001. Melt generation at very slow-spreading oceanic ridges: Constraints from geochemical and geophysical data. *Journal of Petrology* 42, 1171–1196. doi:10.1093/petrology/42.6.1171.
- Zhong, S., Gurnis, M., 1993. Dynamic feedback between a continentlike raft and thermal convection. *Journal of ⁴⁶⁵ Geophysical Research* 98, 12219–12232. doi:10.1029/93JB00193.

Acknowledgements

This research was supported by a BP-Cambridge collaboration. MJH acknowledges support from the National Aeronautics and Space Administration grant NNX17AE17G. OS was supported by Trinity College Cambridge. We are grateful to ION Geophysical for permission to publish the reflection profile shown in Figure 1 from their PelotasSPAN™ dataset. We thank A. Bump, R. Corfield, A. Crosby, I. Frame, D. Glassey, T. Heyn, B. Horn, S. Kisim, C. Langmuir, D. Lyness, L. Mackay, K. McDermott, E. Stirling, M. Thompson and J. Winterbourne for their help. We are grateful to P. Brandl for sharing geochemical analyses and A. Lenardic for insightful feedback at the AGU 2014 poster. Figures were prepared using Generic Mapping Tools. Earth Sciences contribution esc.XXXX. The authors declare no competing financial interests. Data reported in this paper are available online in the Supporting Information.

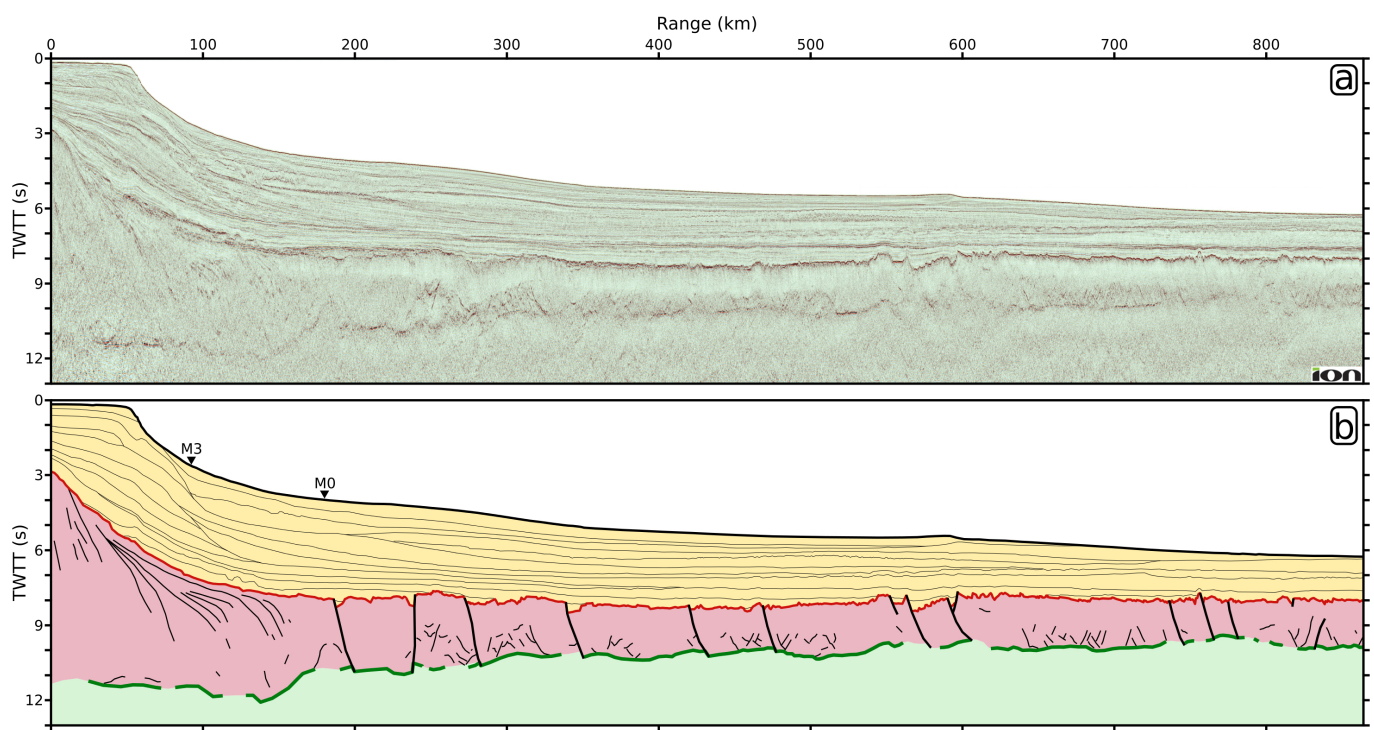


Figure 1: **Oceanic crust example.** (a) Seismic reflection profile from the Pelotas Basin of south Brazil shown courtesy of ION Geophysical Corporation; TWTT = two-way travel time. (b) Interpretation; yellow = sediments; red = igneous basement; green = lithospheric mantle; thick black lines = major normal faults; thin lines = additional structure including seaward-dipping reflectors in basement at left end; labelled black triangles = magnetic anomaly picks (Rabinowitz and LaBrecque, 1979).

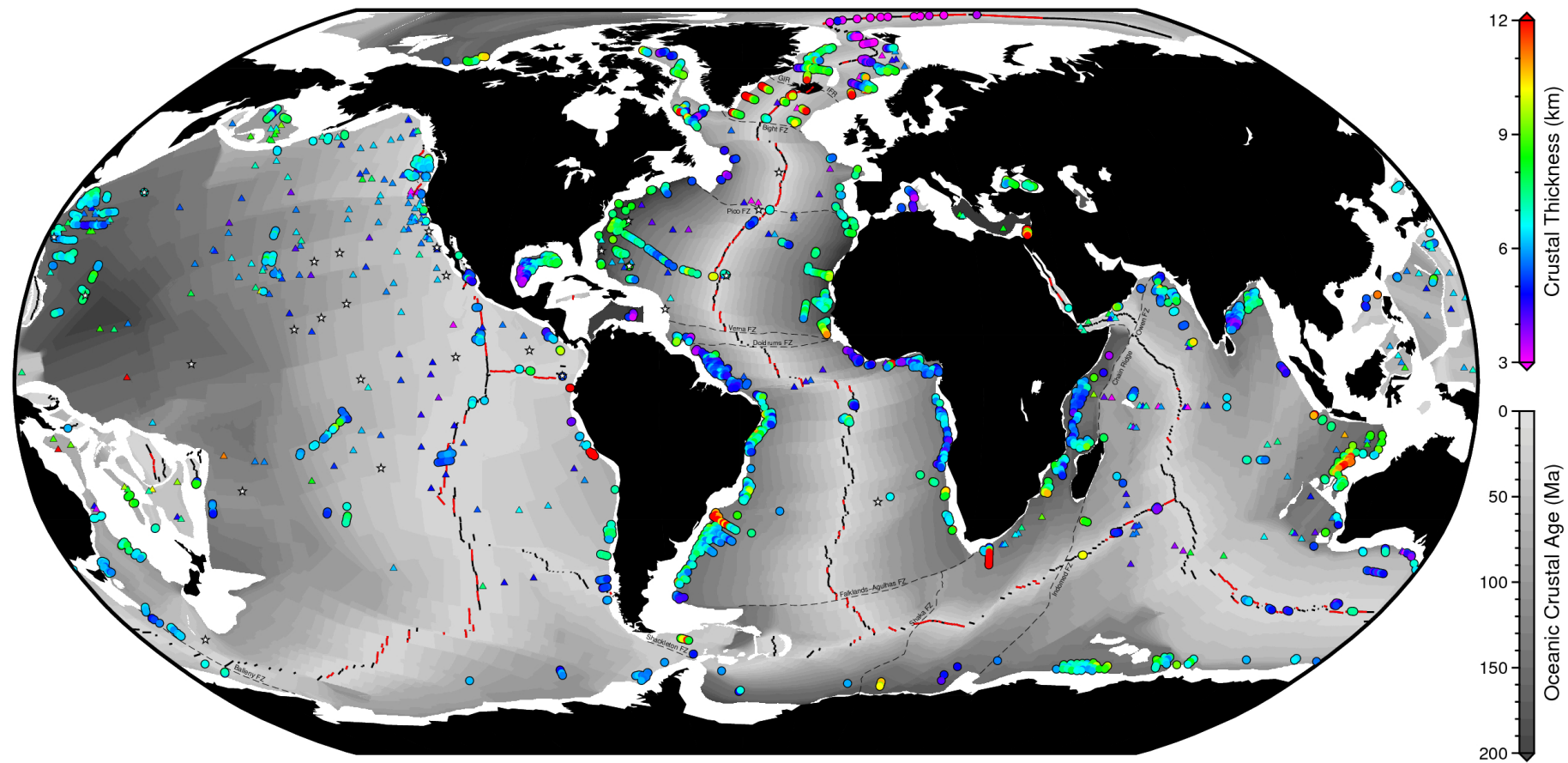


Figure 2: **Map of oceanic crust datasets.** Grey background grid = crustal age from magnetic reversal history (Müller et al., 2016); coloured circles = 2340 accurate crustal thickness measurements averaged in 0.5° bins; triangles = 359 minimum constraints; thick black lines = mid-oceanic spreading centres; red lines = segments with geochemical samples (Gale et al., 2014); stars = drilled basement samples with geochemical analyses (Brandl et al., 2013); thin dashed black lines = bathymetric features used to separate basins; FZ = fracture zone; GIR = Greenland-Iceland Rise; IFR = Iceland-Faeroe Rise.

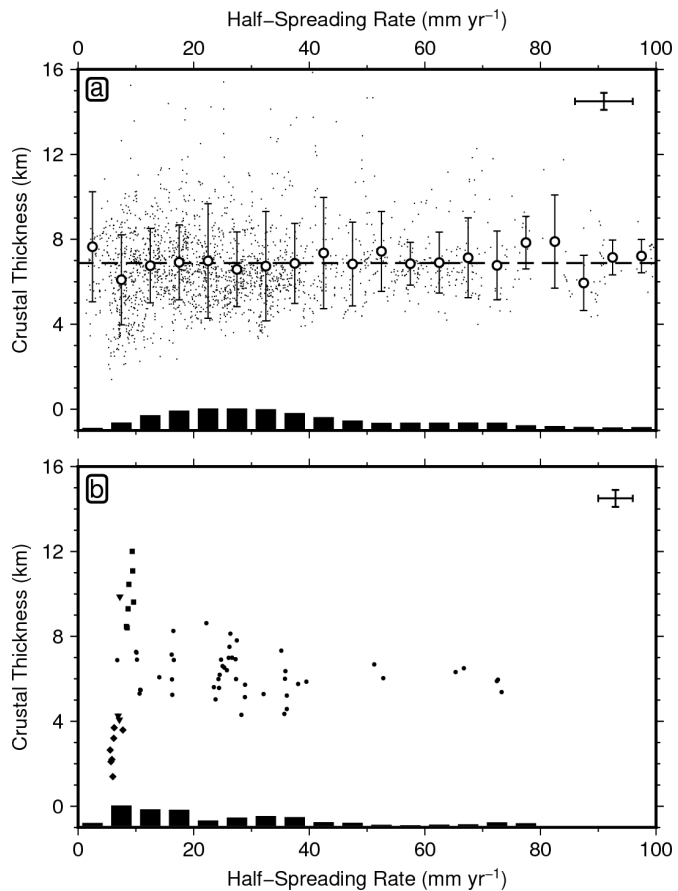


Figure 3: **Crustal thickness versus spreading rate.** (a) Points = 2340 accurate measurements of oceanic crustal thickness (circles in Figure 2) as a function of half-spreading rate (Müller et al., 2008); top-right crosshair = approximate measurement uncertainties; circles with error bars = mean and standard deviation of thickness within 5 mm yr^{-1} bins; dashed line = average crustal thickness of 6.88 km; histogram = total global area of oceanic lithosphere per bin from the grid of Müller et al. (2008). (b) 66 segment-averaged, accurate thickness measurements on crust younger than 10 Ma and closer than 200 km to the ridge as a function of present-day ridge half-spreading rate (Gale et al., 2013); squares = subset of 7 segments within 1000 km of Iceland; diamonds = subset of 7 segments on the Mohns and Gakkel ridges; triangles = subset of 3 segments on the Southwest Indian Ridge; histogram = total global length of active ridge per bin.

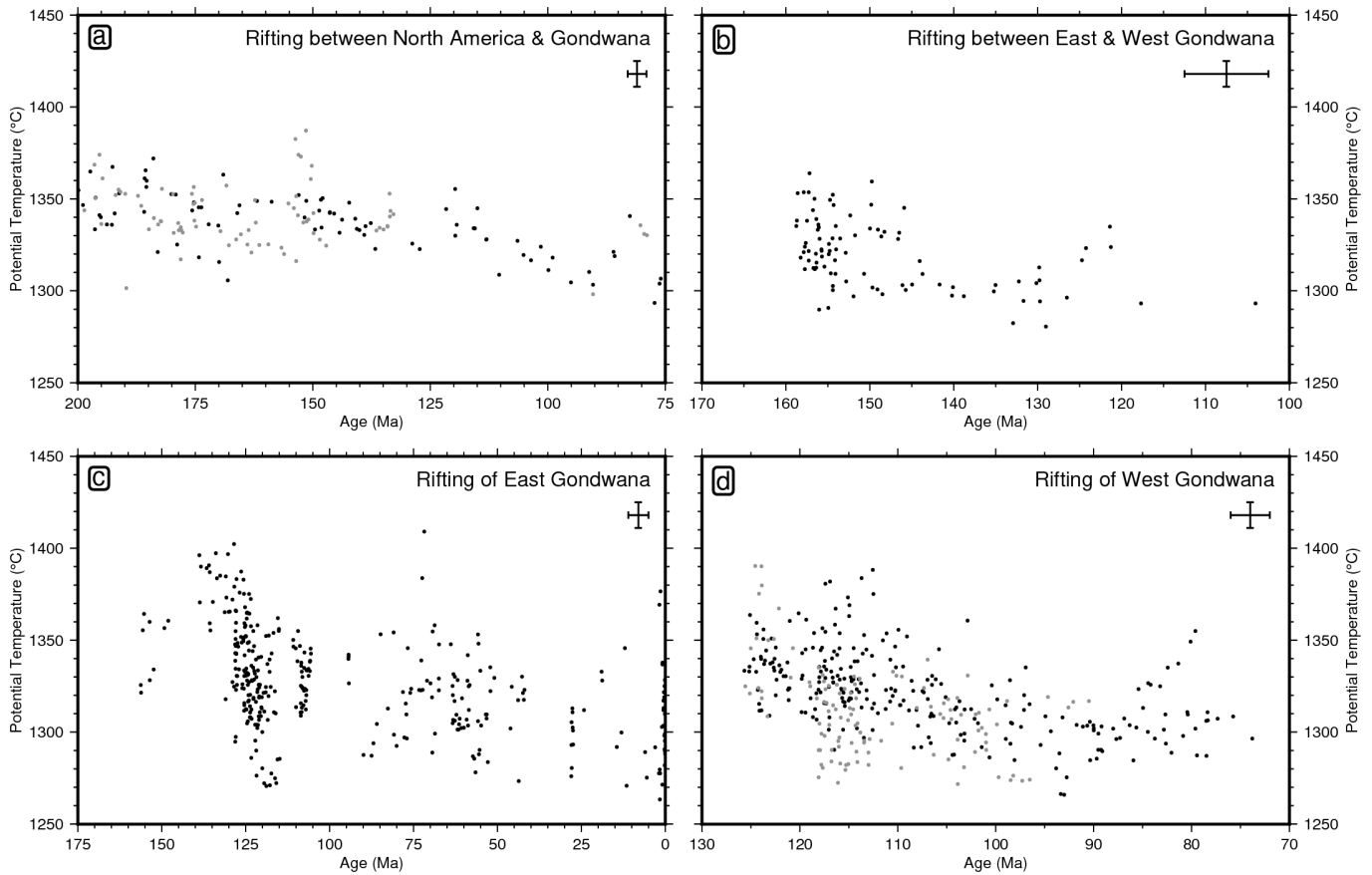


Figure 4: Potential temperature through time for break-up of Gondwana. (a) Rifting of North America from Gondwana. Circles = accurate measurements of oceanic crustal thickness (circles in Figure 2); black = data from North American side of present-day Mid-Atlantic Ridge; grey = data from African side; top-right crosshair shows typical measurement uncertainty. (b) Break-up of East and West Gondwana to form the present-day Somali-Tanzanian Basins and Mozambique Channel. (c) Rifting of East Gondwana to form the majority of the present-day Indian Ocean. (d) Break-up of West Gondwana forming the present-day South Atlantic Ocean. Black = data from South American side of present-day Mid-Atlantic Ridge; grey = data from African side.

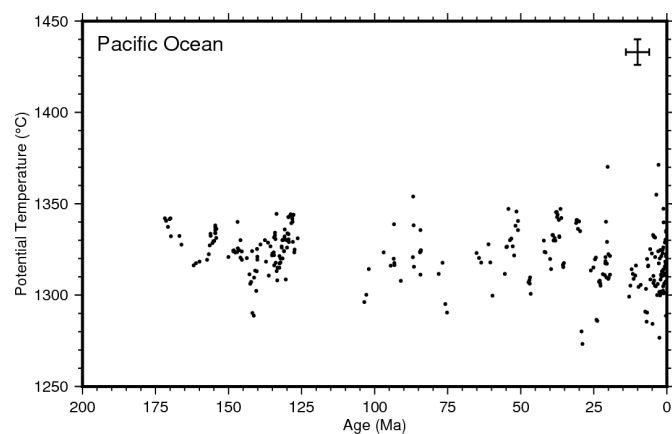


Figure 5: Potential temperature through time for Pacific Ocean. Circles = accurate measurements of oceanic crustal thickness (circles in Figure 2); top-right crosshair shows typical measurement uncertainty.

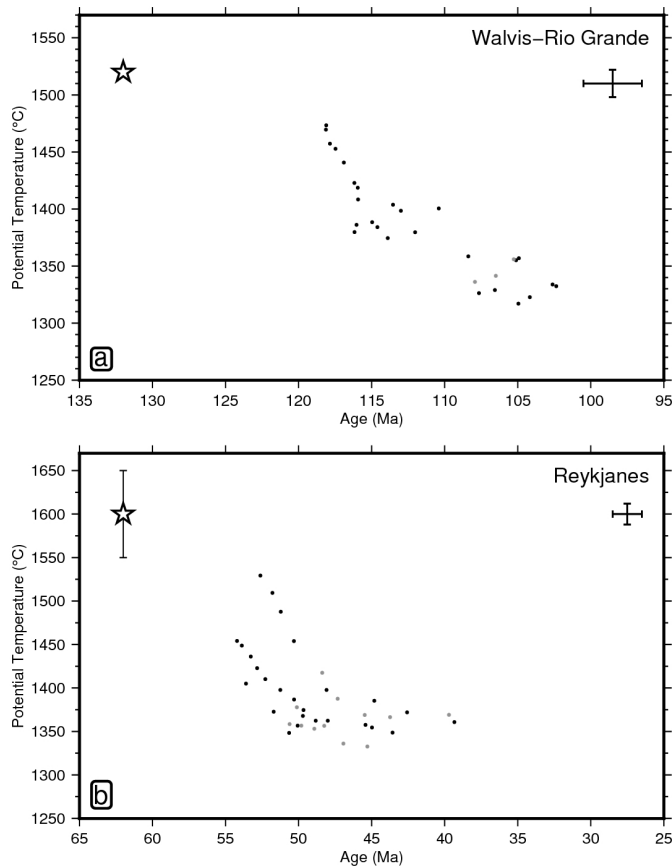


Figure 6: Potential temperature through time for plume-influenced break-up. (a) Data from the Tristan de Cunha plume. Black = Rio-Grande Rise; grey = Walvis Ridge; top-right shows typical measurement uncertainty. (b) Data south of the Icelandic plume. Black = Greenland; grey = Faeroe margin.

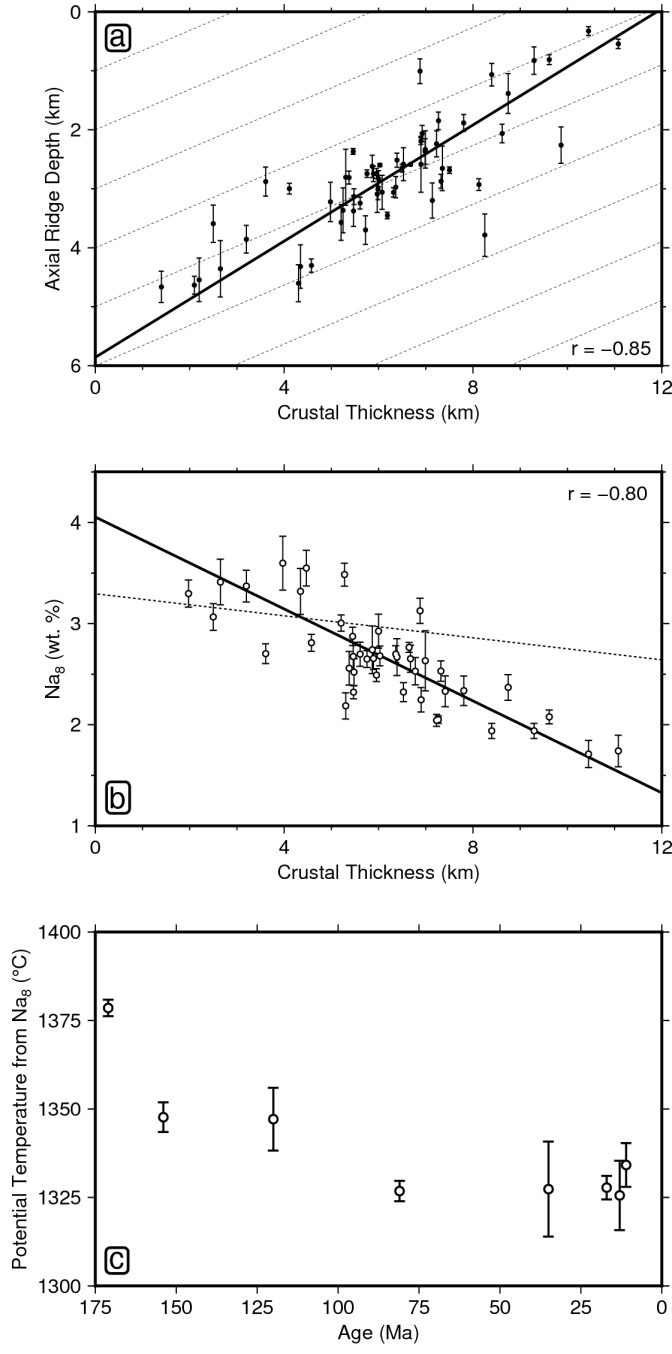


Figure 7: Crustal thickness versus geochemistry. (a) 61 segment-averaged crustal thickness measurements on crust younger than 5 Ma versus mean and standard deviation of axial ridge depth from Gale et al. (2013); typical crustal thickness uncertainty = $\pm 5\%$; solid line = linear best fit with Pearson's correlation coefficient $r = -0.85$; dashed lines = expected relationship given simple isostasy. (b) Subset of 45 of these measurements within 300 km of a ridge segment with associated segment-averaged Na_8 values and 1σ uncertainty (Gale et al., 2014); solid line = best fit relationship with Pearson's correlation coefficient $r = -0.80$; dashed line = approximate relationship used by Brandl et al. (2013). (c) 8 Na_8 values with 1σ uncertainty from Atlantic drill sites (Brandl et al., 2013), converted into potential temperature using new relationship from (b).

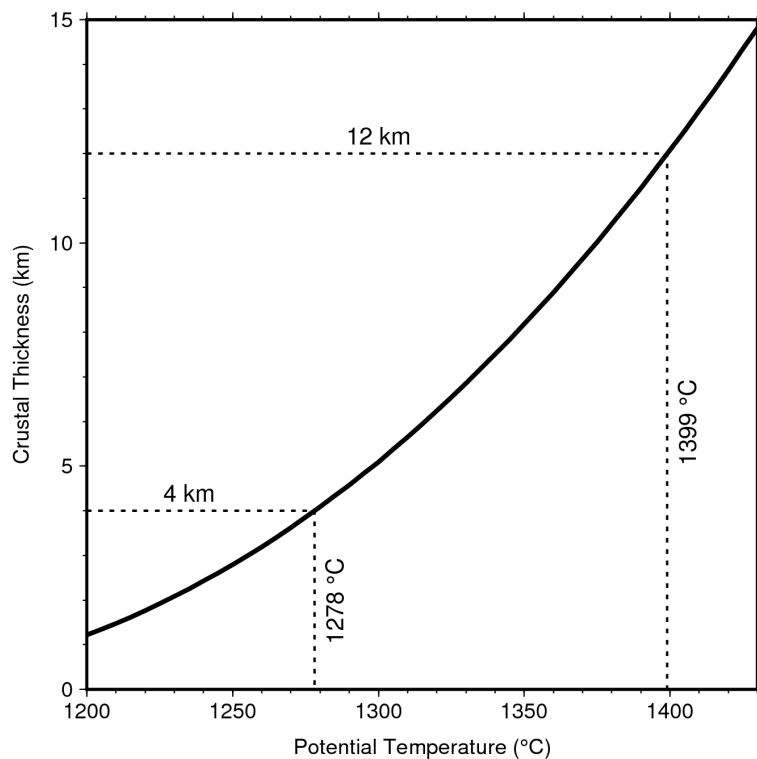
Melting Model

Figure S1: **Melting model.** Igneous crustal thickness from the melting parameterisation of Shorttle et al. (2014), using the solidus and liquidus of the KLB-1 lherzolite lithology (Katz et al., 2003).

Zoomed Crustal Thickness Maps

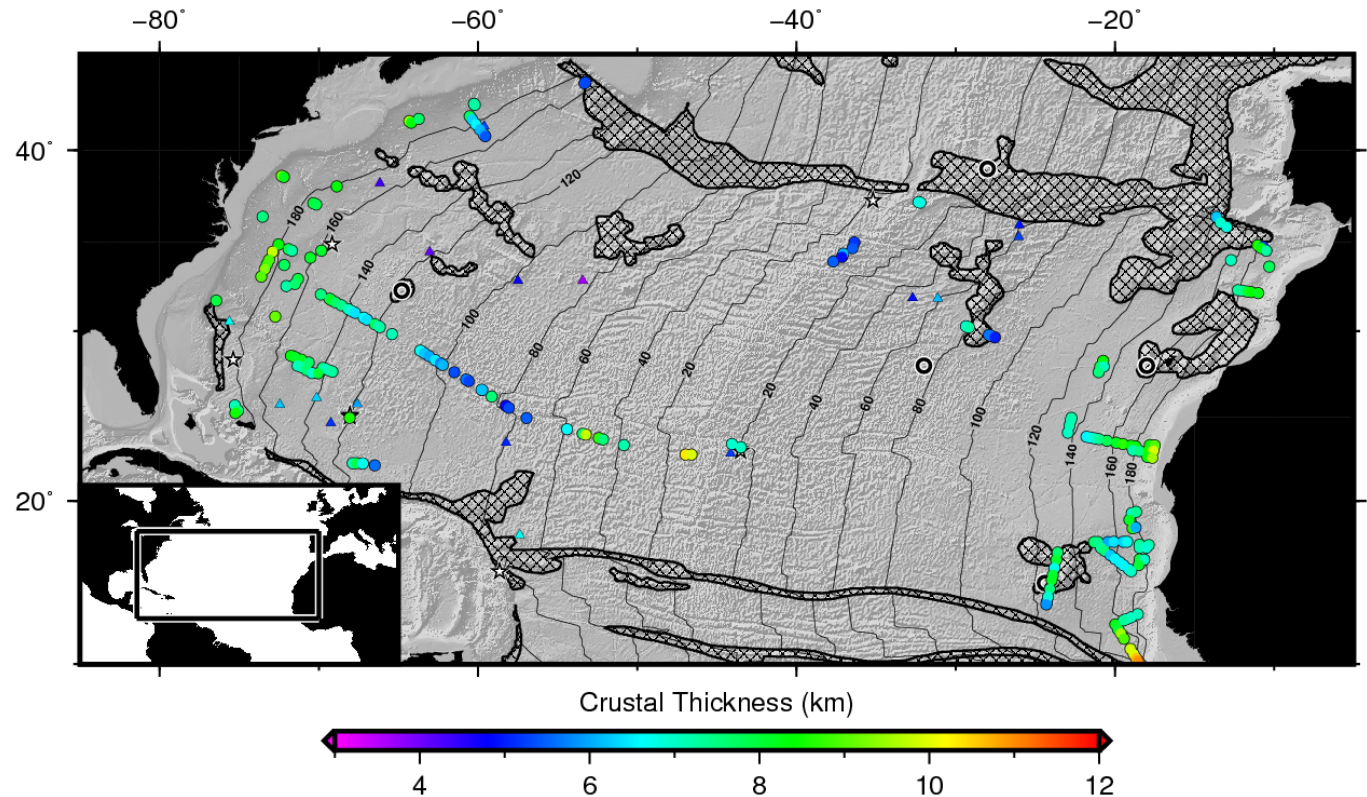


Figure S2: **Oceanic crustal thickness measurements in Central Atlantic Ocean.** Coloured circles/triangles = accurate/minimum crustal thickness measurements; greyscale = hillshade of ETOPO2 bathymetry (NGDC, 2006); black lines = crustal age contours labelled in Ma from magnetic reversal history (Müller et al., 2016); black rings = Neogene magmatic hotspots; black stars = drill sites with MORB samples (Brandl et al., 2013).

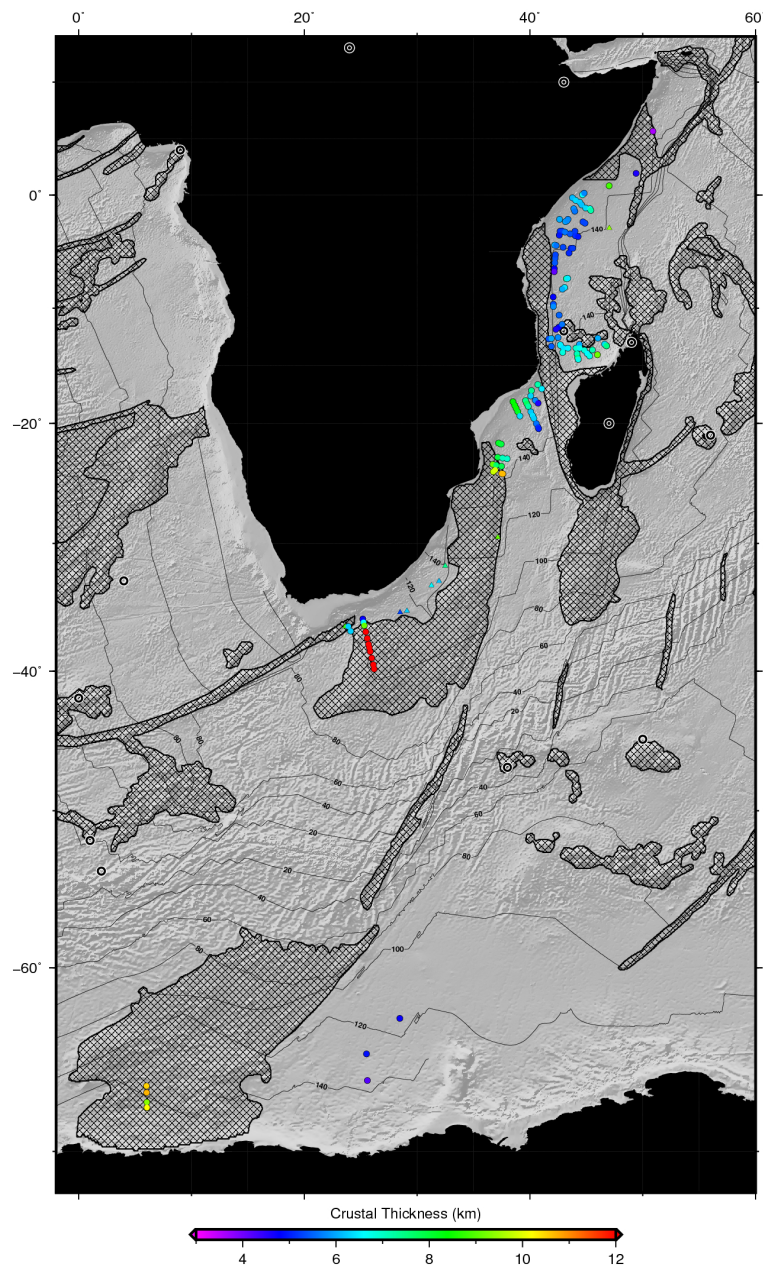


Figure S3: **Oceanic crustal thickness measurements on East African lithosphere.** Coloured circles/triangles = accurate/minimum crustal thickness measurements; greyscale = hillshade of ETOPO2 bathymetry (NGDC, 2006); black lines = crustal age contours labelled in Ma from magnetic reversal history (Müller et al., 2016); black rings = Neogene magmatic hotspots.

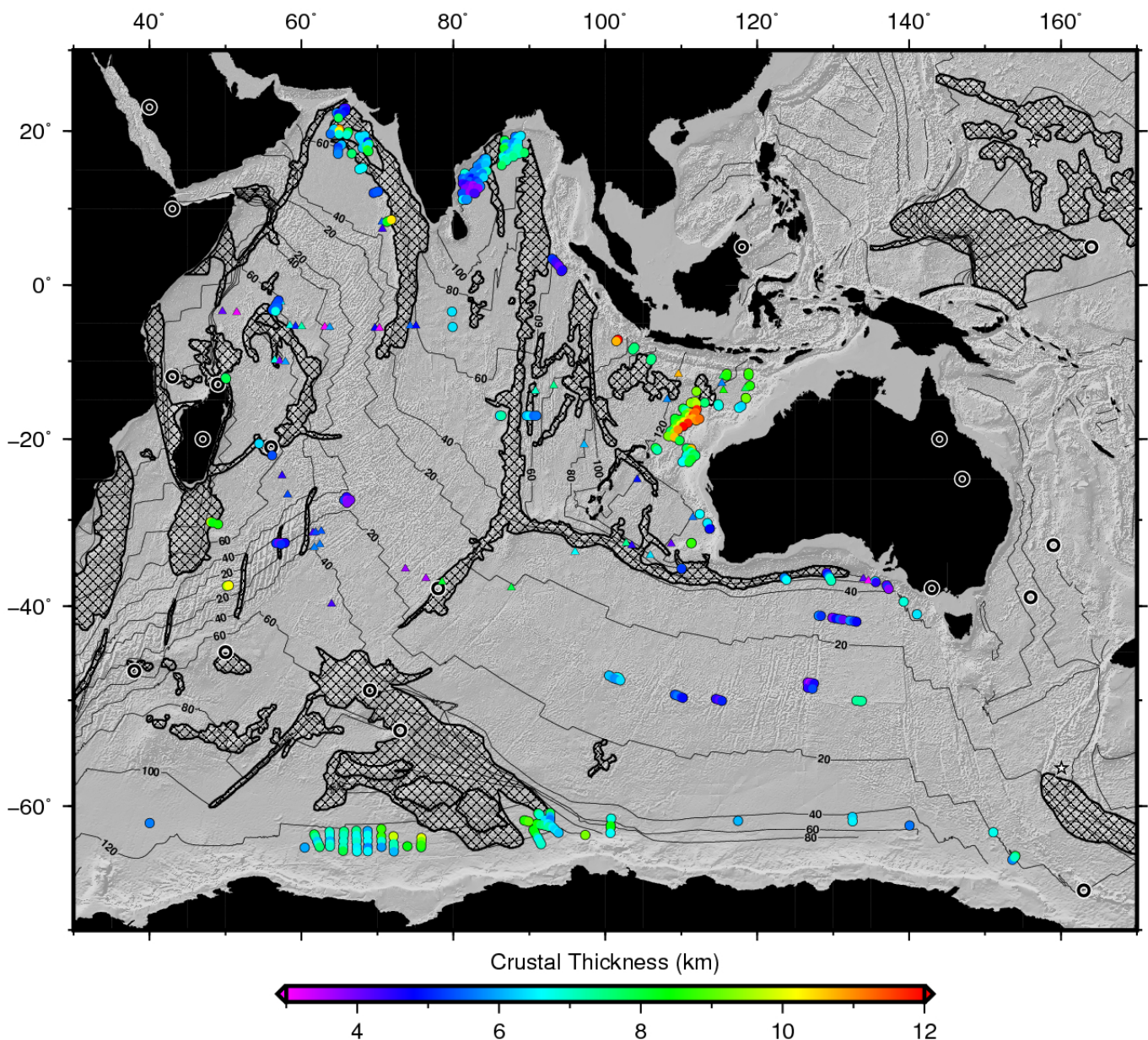


Figure S4: **Oceanic crustal thickness measurements in Indian Ocean.** Coloured circles/triangles = accurate/minimum crustal thickness measurements; greyscale = hillshade of ETOPO2 bathymetry (NGDC, 2006); black lines = crustal age contours labelled in Ma from magnetic reversal history (Müller et al., 2016); black rings = Neogene magmatic hotspots.

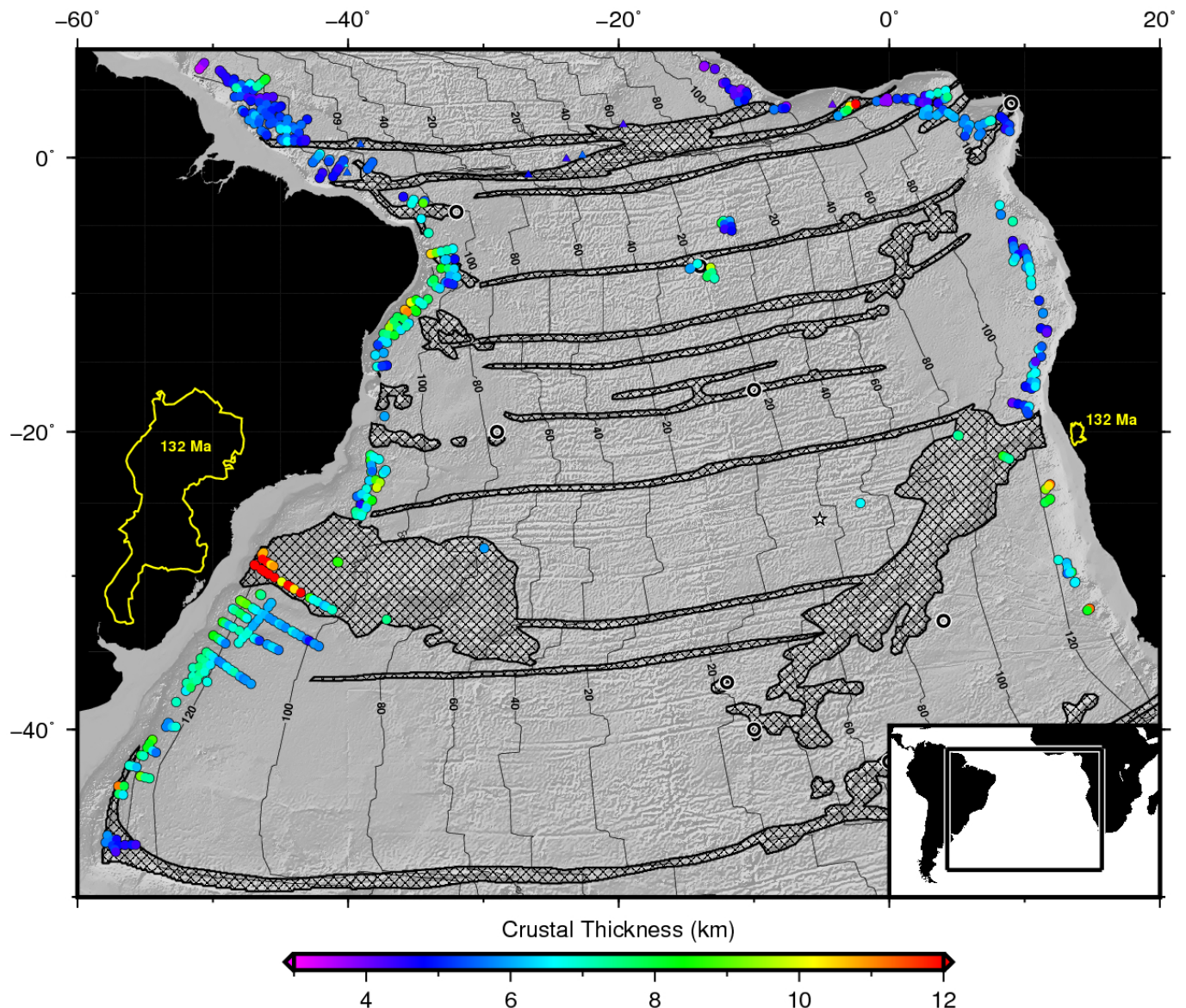


Figure S5: **Oceanic crustal thickness measurements in South Atlantic Ocean.** Coloured circles/triangles = accurate/minimum crustal thickness measurements; greyscale = hillshade of ETOPO2 bathymetry (NGDC, 2006); cross-hatched polygons = major fracture zones and seamounts; black lines = crustal age contours labelled in Ma from magnetic reversal history (Müller et al., 2016); black rings = Neogene magmatic hotspots; yellow polygons = extent of Paraná-Etendeka flood basalts; black star = drill site with MORB sample (Brandl et al., 2013).

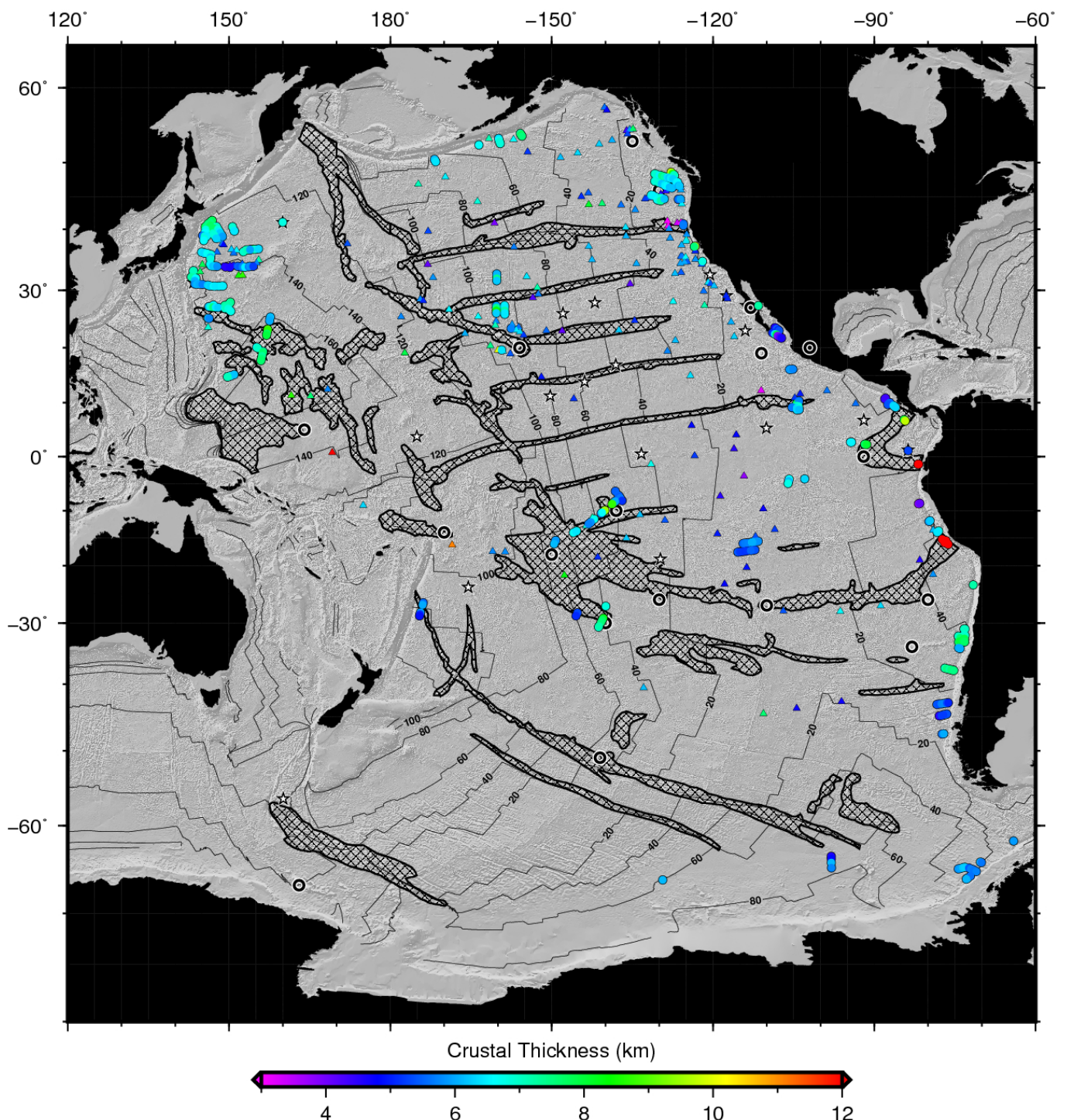


Figure S6: Oceanic crustal thickness measurements in Pacific Ocean. Coloured circles/triangles = accurate/minimum crustal thickness measurements; greyscale = hillshade of ETOPO2 bathymetry (NGDC, 2006); cross-hatched polygons = major fracture zones and seamounts; black lines = crustal age contours labelled in Ma from magnetic reversal history (Müller et al., 2016); black rings = Neogene magmatic hotspots; black stars = drill sites with MORB samples (Brandl et al., 2013).

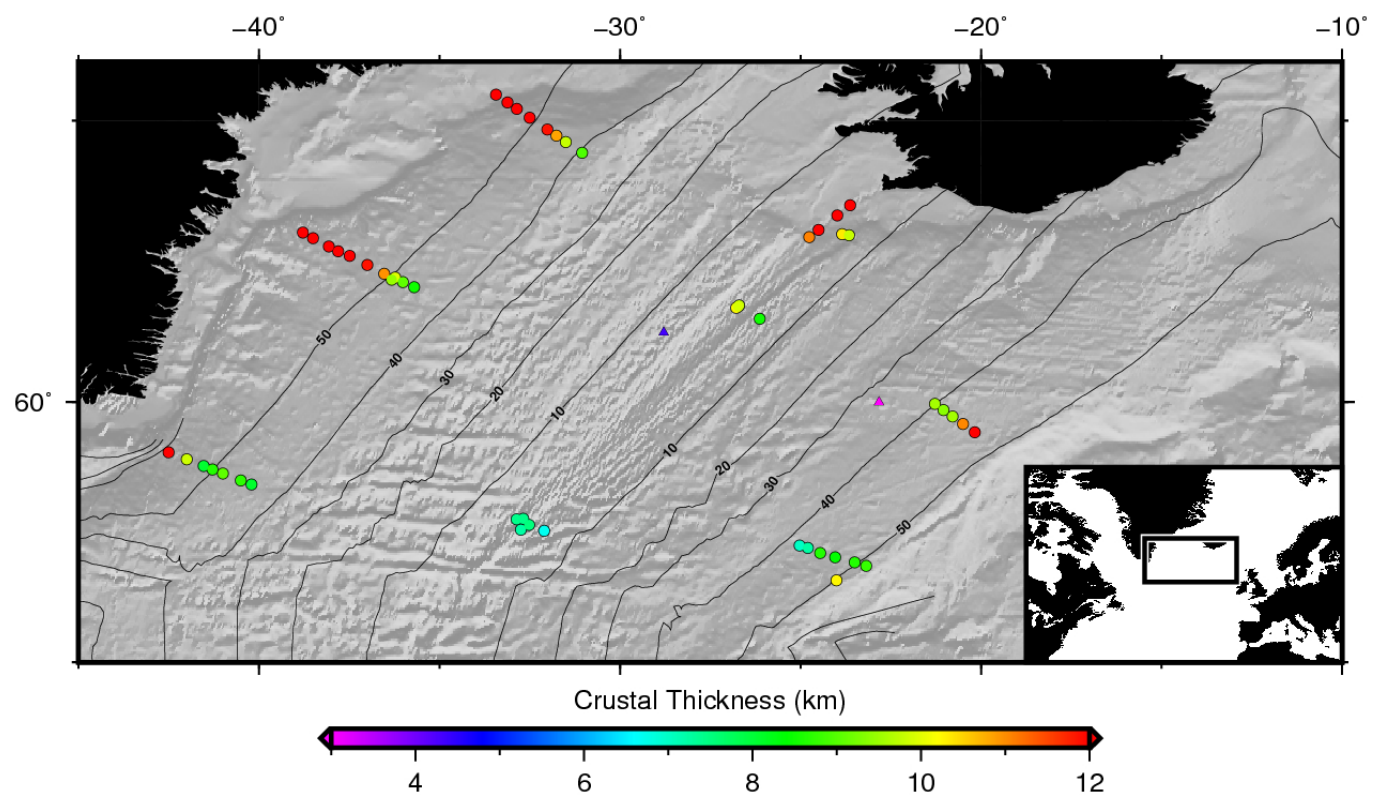


Figure S7: **Oceanic crustal thickness measurements in North Atlantic Ocean.** Coloured circles/triangles = accurate/minimum crustal thickness measurements; greyscale = hillshade of ETOPO2 bathymetry (NGDC, 2006); black lines = crustal age contours labelled in Ma from magnetic reversal history (Müller et al., 2016).

Crustal Thickness versus Ridge Geochemistry

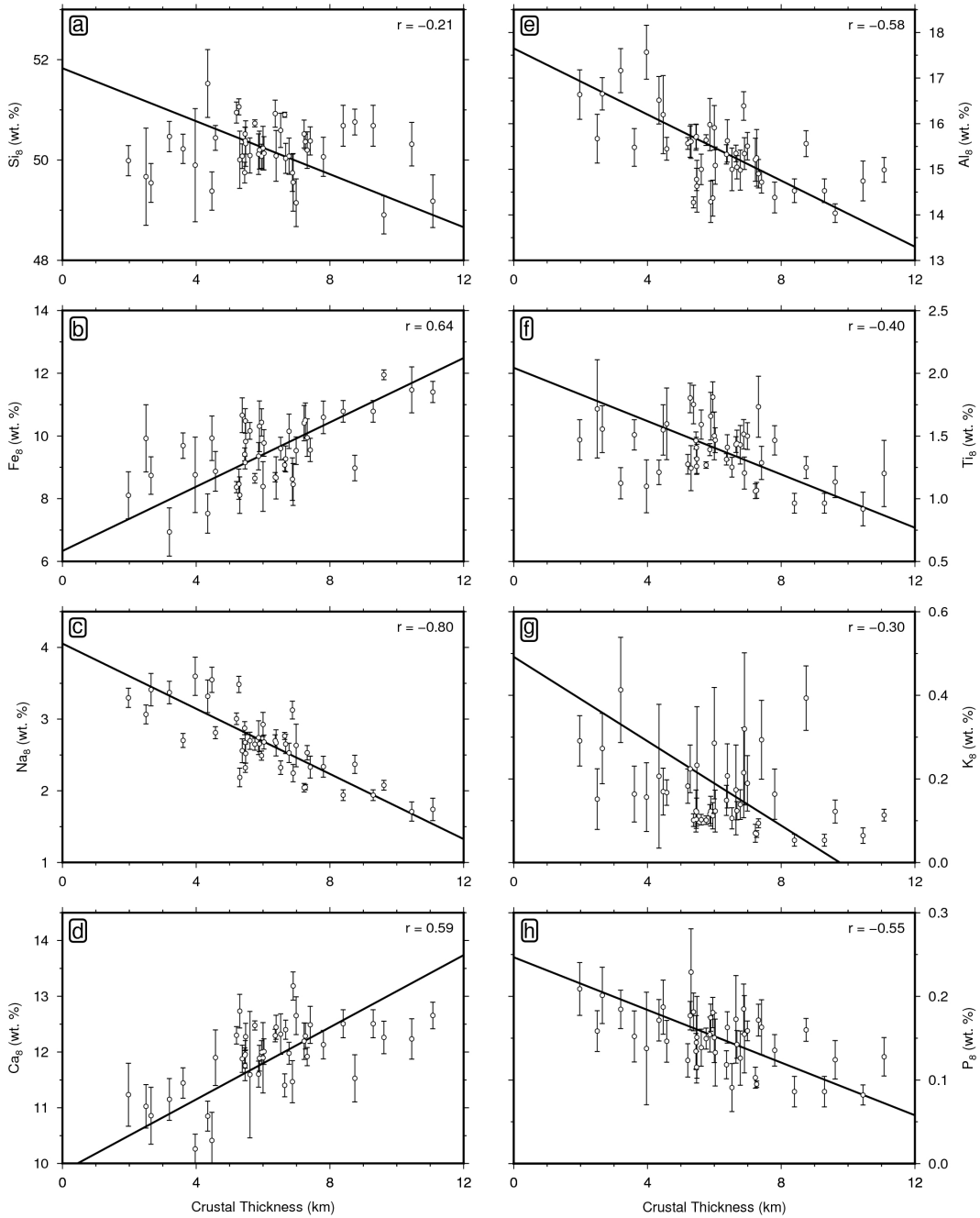


Figure S8: **Crustal thickness versus ridge geochemistry.** (a) 33 segment-averaged crustal thickness measurements on crust younger than 1 Ma within 200 km of a segment with geochemical analyses from Gale et al. (2014); circles with error bars represent mean and standard deviation of Si_8 wt. %; r = Pearson's correlation coefficient. (b) Same for Fe_8 . (c) Na_8 . (d) Ca_8 . (e) Al_8 . (f) Ti_8 . (g) K_8 . (h) P_8 .